

Target decomposition and recognition from wide-angle SAR imaging based on a Gaussian amplitude-phase model

Yongchen LI & Ya-Qiu JIN*

Key Laboratory for Information Science of Electromagnetic Waves, Fudan University, Shanghai 200433, China

Received October 27, 2016; accepted December 12, 2016; published online March 1, 2017

Abstract Wide-angle synthetic aperture radar (W-SAR) imaging accounts for multi-azimuthal scattering and is feasible for retrieving more comprehensive features of complex targets. Because a typical target is seen as composed of its components (typically, some simple geometric objects), a Gaussian amplitude-phase (GAP) model has been developed for the analysis of multi-azimuthal scattering from these objects. Based on the time-frequency analysis of wide-angle scattering, the parameters of the GAP model were estimated, including the Gaussian variance, the surface curvature, and the number of objects in all imaged pixels. Numerical simulations and real measurements demonstrate the capability of the GAP model for decomposing and recognizing complex electric-large targets.

Keywords wide-angle SAR, Gaussian amplitude-phase, time-frequency, target decomposition, target recognition

Citation Li Y C, Jin Y-Q. Target decomposition and recognition from wide-angle SAR imaging based on a Gaussian amplitude-phase model. *Sci China Inf Sci*, 2017, 60(6): 062305, doi: 10.1007/s11432-016-0572-3

1 Introduction

Wide-angle synthetic aperture radar (W-SAR) integrates multi-aspect observations in the azimuthal direction, which may improve the azimuthal resolution and yield comprehensive scattering features of complex targets [1]. Usually, a complex target yields diverse azimuthal scattering data, with each imaged pixel likely containing information on scattering from several structural components of the target. Thus, analysis of W-SAR imaging data can sensitively determine target structural classification and recognition of complex targets.

Feature classification by wide-angle imaging have been extensively studied, mostly in terms of sub-aperture and time-frequency analysis [1–10]. Scattering persistence and azimuthal diversity in wide-angle imaging were discussed. However, all of these approaches lack quantitative models to describe the scattering diversity of widely imaged features.

In this paper, we present a Gaussian amplitude-phase (GAP) parameterized model and represents a complex electric-large (e-large) target as composed of simple geometric objects. Using time-frequency

* Corresponding author (email: yqjin@fudan.edu.cn)

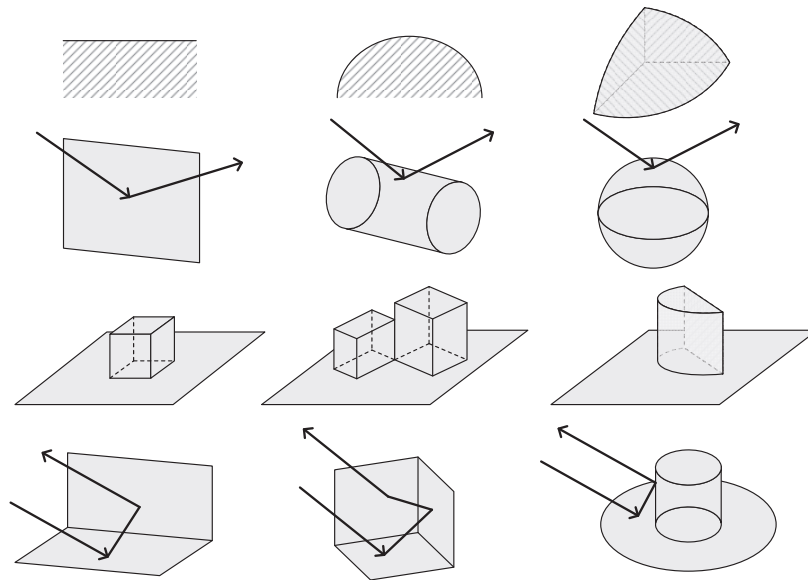


Figure 1 Illustration of scattering mechanisms for simple geometric objects.

analysis to obtain the index spectrogram, the parameters of the GAP model were retrieved, including the Gaussian variance, the surface curvature, and the number of objects for all W-SAR imaged pixels. In the GAP model, the variance represents the scattering persistence in the azimuthal direction, related to the object length or curvature; the curvature distinguishes flat surfaces from curved ones; and the number of objects accounts for the overlapping scatterers. The retrieved GAP model parameters were then used for decomposing and recognizing complex targets.

This paper is organized as follows. Section 2 describes a geometric approximation of scattering mechanisms. Section 3 develops the GAP model for a general complex target composed of simple geometric objects. In Section 4, the Gabor transform of time-frequency analysis is applied for obtaining the azimuthal spectrogram for W-SAR imaging, following which the GAP parameters are estimated for each imaged pixel. In Section 5, wide-angle scattering data from numerical simulations and real measurements are applied to validate the GAP model for classifying complex targets. Finally, discussion and conclusion are provided in Section 6.

2 Geometric approximation of scattering mechanisms

A complex e-large target may yield many scattering mechanisms, whose basic geometries are described in Figure 1. Figure 1 illustrates the scattering from simple geometric objects owing to different scattering mechanisms. For example, specular scattering from a plane can be described by a plate, while scattering from one- and two- curved surfaces can be described by a cylinder and a sphere, respectively. Multiple reflections yield multi-scattering, as shown in Figure 1. Double scattering between a cube and ground is represented by a dihedral, triple scattering among two intersected cubes and the ground is described by a trihedral, and double scattering between a curved object and the ground is described by a top-hat. Here, very small edge diffraction and travelling waves are usually negligible.

Scattering from simple objects can be analytically calculated based on the geometrical optics (GO) or physical optics (PO) [11]. Under the high-frequency approximation, the entire scattering from an e-large target is contributed by these objects, i.e., local scattering centers [12]. As shown in Figure 2, a very complex vessel can be seen as composed of simple objects, e.g., two vertical planes as a dihedral, three vertical planes as a trihedral, the helicopter on the deck as a dihedral, the turret and the radar radome as a top-hat, the radome on the tower as a sphere, and the fence around the deck as thin wires. Note that some scattering caused by cavities or surface creeping waves is very small and usually can be neglected.

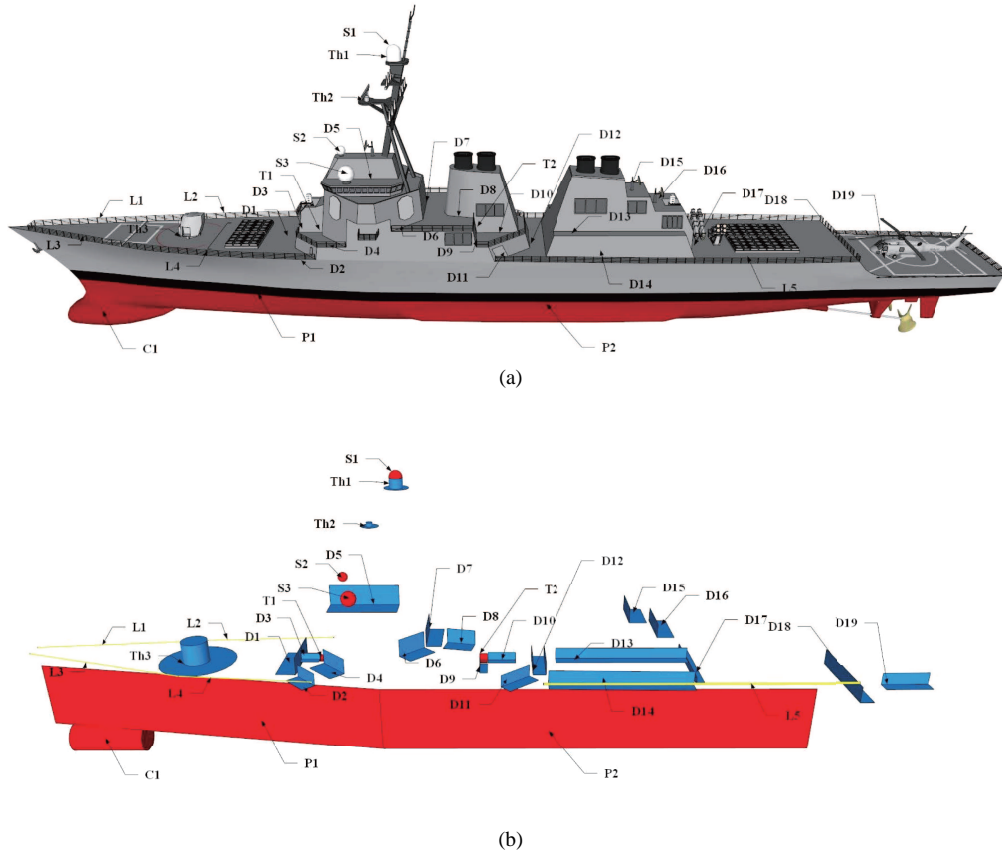


Figure 2 (Color online) The vessel model and its decomposition. (a) The vessel model; (b) decomposed objects (S: sphere, Th: top-hat, T: trihedral, D: dihedral, L: line, and P: plate).

3 Gaussian basis of azimuthal scattering from simple geometric objects

The angular pattern of scattering is closely related to the scatterer size, shape, and orientation. In addition, a curved-surface object may shift the scattering phase owing to its radius [11]. Extracting the features of these objects is usually difficult owing to high-order modelling and sensitivity of parameter initialization [13]. We developed a simplified GAP model with the Gaussian basis to describe scattering from simple geometric objects. The Gaussian function for modeling the scattering-related features has been discussed in detail [14–16]. Here, we adopted the Gaussian basis for characterizing the azimuthal scattering-based imaging of simple geometric objects.

3.1 Gaussian basis for the amplitude response

It has been shown that the angular pattern of scattering from simple geometric objects may vary as a sinc(\cdot), sin(\cdot), cos(\cdot) function, or may remain invariant, depending on the object type [11]. The scattering amplitude can be approximated as a Gaussian function with variance corresponding to the azimuthal angle. For example, let the lengths of a plate, a dihedral, and a horizontal cylinder be 15λ , 10λ , 5λ , respectively. Figure 3 shows the main scattering lobes (marked curves), and the dashed curves are the corresponding Gaussian fits to the main scattering lobes within the azimuthal width of 20° . The scattering from a trihedral is also shown in Figure 3. The standard deviations (stds) and the relative errors for the fits in Figure 3 are listed in Table 1.

It can be seen that all main scattering lobes, for the four types of objects, are satisfactorily fitted by Gaussian functions. The standard deviation indicates the scattering persistent width in the azimuthal direction, which may be used for identifying the objects, e.g., trihedrals have large standard deviations while plates have small standard deviations. The standard deviation may represent the azimuthal dis-

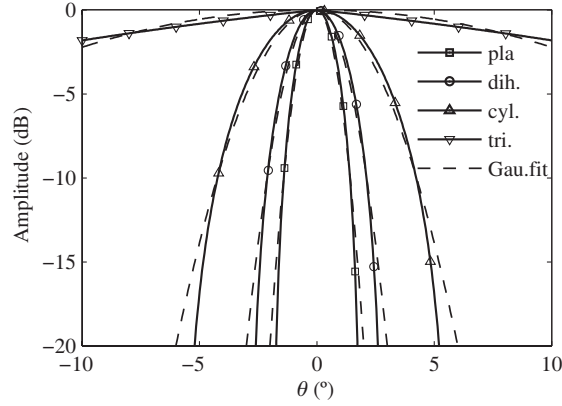


Figure 3 Gaussian fits to the main lobe scattering curves for simple objects.

Table 1 Standard deviations and relative errors of Gaussian fits to scattering curves, for different objects

Type	Plate	Dihedral	Cylinder	Trihedral
Std.	0.0163	0.0244	0.0488	0.2440
Relative err. (%)	0.06	0.09	0.17	0.03

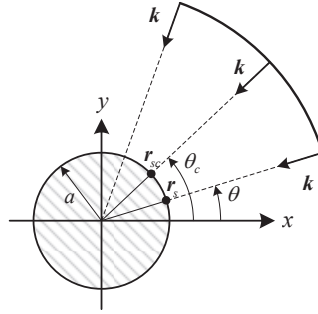


Figure 4 Incident azimuth on a cylinder surface.

persed width of the scattering amplitude, whose mean value indicates the object's orientation. Thus, a Gaussian basis function for amplitude response is defined as

$$A(\theta) = \exp[-(\theta - \theta_o)^2/2\sigma^2], \quad (1)$$

where the variance σ denotes the scattering persistence, and θ_o indicates its orientation.

Note that the sphere and top-hat exhibit invariant scattering with respect to the azimuth. Usually, a Gaussian model with a large variance is also taken as a model of a curved-surface object, e.g., a sphere or a top-hat.

3.2 Gaussian basis for the phase shift

Planar-surface objects, e.g., a plate, a dihedral and a trihedral, do not cause scattering-induced phase shift, and their geometric centers coincide with scattering centers. However, curved-surface objects, e.g., a sphere, a cylinder, and a top-hat, yield some phase shift on scattering and shift the scattering centers relative to their geometric centers.

With respect to the geometric center in Figure 4, a phase shift owing to the scattering from a cylinder is

$$\Delta\phi = 2\mathbf{k} \cdot \mathbf{r}_s = 2ka, \quad (2)$$

where $\mathbf{r}_s = a[\cos\theta, \sin\theta]^T$ is a sliding point, and $\mathbf{k} = k[\cos\theta, \sin\theta]^T$ is the incident wave vector.

Under a small angle approximation $\cos(\theta - \theta_c) \approx 1 - (\theta - \theta_c)^2/2$, and Eq. (2) at the center of the incident angle span can be written as

$$\Delta\phi = 2\mathbf{k} \cdot \mathbf{r}_{sc} + 2\mathbf{k} \cdot (\mathbf{r}_s - \mathbf{r}_{sc}) \approx 2\mathbf{k} \cdot \mathbf{r}_{sc} + ka(\theta - \theta_c)^2, \quad (3)$$

where \mathbf{r}_{sc} represents a focused scattering center position on the cylinder surface rather than its geometric center, while $ka(\theta - \theta_c)^2$ yields a small positional shift for \mathbf{r}_{sc} .

Without loss of generality, the position of a scattering center, $\mathbf{r} = [x, y]^T$, is defined to account for both planar-surface and curved-surface objects. For a planar surface object, the scattering center \mathbf{r} is located at the object's geometric center, while for a curved-surface object, \mathbf{r} is located at the focused scattering center on the object's surface. Thus, in general, the scattering phase ϕ for an object is written as

$$\phi = 2\mathbf{k} \cdot \mathbf{r} + ka(\theta - \theta_c)^2, \quad (4)$$

where $ka(\theta - \theta_c)^2$ is a special phase modulation for curved-surface objects.

To combine the amplitude and phase Gaussian basis, the GAP model is presented as

$$S(k, \theta) = A \exp\{-(\theta - \theta_o)^2/2\sigma^2 - i[2\mathbf{k} \cdot \mathbf{r} + ka(\theta - \theta_c)^2]\}, \quad (5)$$

where θ_o, σ, a can be seen as the object's attributes and the parameter A accounts for the scattering contribution of the GAP model to the overall scattering.

3.3 Scattering center shift

The phase modulation $\phi_m = ka(\theta - \theta_c)^2$ of the GAP model shifts the scattering center in the time domain. In the $x_s - y_s$ coordinate, with the incident direction along the x_s axis, this shift is written as $\mathbf{r}_{\text{shift}} = [\Delta x, \Delta y]^T$,

$$\Delta x = c\Delta t/2, \quad \Delta y = \lambda f_d/2\Omega. \quad (6)$$

The shift Δx in the range direction is related to the echo delay Δt , and the shift Δy is related to the Doppler frequency, where $\Omega = d\theta/dt$ and

$$\Delta t = -\frac{1}{2\pi} \frac{d\phi_m}{df} = a(\theta - \theta_c)^2, \quad f_d = -\frac{1}{2\pi} \frac{d\phi_m}{dt} = 2\Omega a(\theta - \theta_c)/\lambda. \quad (7)$$

Substituting (7) into (6), we obtain that the scattering center moves by

$$\mathbf{r}_{\text{shift}}(\theta) = \begin{bmatrix} \Delta x \\ \Delta y \end{bmatrix} = \begin{bmatrix} a(\theta - \theta_c)^2/2 \\ a(\theta - \theta_c) \end{bmatrix}. \quad (8)$$

Defining the rotation angle τ between the incident coordinate $x_s - y_s$ and the target coordinate $x - y$, and the shift of the scattering center in the target coordinate is written as $\bar{\mathbf{T}}(\tau) \cdot \mathbf{r}_{\text{shift}}(\theta)$, with the rotation matrix

$$\bar{\mathbf{T}}(\tau) = \begin{bmatrix} \cos \tau & -\sin \tau \\ \sin \tau & \cos \tau \end{bmatrix}. \quad (9)$$

4 Gabor transform of the GAP model

To bridge azimuthal scattering in the frequency and time domains, the joint time-frequency analysis has been applied to transform azimuthal scattering to the imaging spectrogram for feature analysis [5–7]. The Gabor transform is a linear time-frequency analysis [17]. The Gabor transform function is defined as

$$G(\theta; \theta_i, \mathbf{r}') = \exp[-(\theta - \theta_i)^2/2\sigma_g^2 - i2\mathbf{k} \cdot \mathbf{r}'], \quad (10)$$

where σ_g is the width of the Gabor window, θ_i is a uniformly discrete angle within $[\theta_{\min} - \sigma_g, \theta_{\max} + \sigma_g]$, and $\mathbf{r}' = [x', y']^T$ denotes the position vector in the time domain. σ_g is related to the azimuthal resolution δ_a of the Gabor transform

$$\sigma_g = \lambda/\sqrt{2}\delta_a. \quad (11)$$

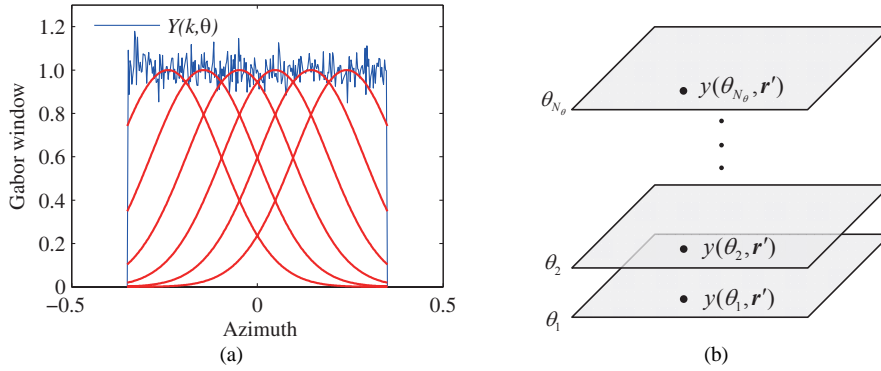


Figure 5 (Color online) Gabor transform from azimuthal scattering to azimuthal spectrogram. (a) Gabor window; (b) azimuth spectrogram.

The Gabor transform of scattering data $Y(k, \theta)$ yields a complex spectrogram at the azimuth θ_i ,

$$y(\theta_i, \mathbf{r}') = \int Y(k, \theta) G^*(\theta; \theta_i, \mathbf{r}') d\mathbf{k}, \quad (12)$$

where the superscript $*$ denotes a conjugate. Thus, a Gabor transform for scattering data can be considered as the scattering imaging with a Gaussian window. A sequential Gabor transform was applied to $Y(k, \theta)$ to obtain spectrograms at the azimuthal angles, $\theta_1, \theta_2, \dots, \theta_{N_\theta}$, and the results are shown in Figure 5, where N_θ is the number of Gabor transforms. Each spectrogram $y(\theta_i, \mathbf{r}')$ corresponds to the scattering imaging at the azimuthal center θ_i . All imaged pixels were stacked at the same position \mathbf{r}' , as indicated by the black dots in Figure 5(b), to form a vector $\mathbf{y} = [y(\theta_1, \mathbf{r}'), y(\theta_2, \mathbf{r}'), \dots, y(\theta_{N_\theta}, \mathbf{r}')]^T$, which represents a spectral line at one imaged pixel.

Similarly, a Gabor transform was applied to (5) as well as imaging with a Gaussian window

$$\begin{aligned} s(\theta_i, \mathbf{r}') &= \int S(k, \theta) G^*(\theta; \theta_i, \mathbf{r}') d\mathbf{k} \\ &= A \int \exp[-(\theta - \theta_o)^2/2\sigma^2 - (\theta - \theta_i)^2/2\sigma_y^2] \exp[i2\mathbf{k} \cdot (\mathbf{r}' - \mathbf{r}) - ika(\theta - \theta_c)^2] d\mathbf{k}. \end{aligned} \quad (13)$$

Substituting $\theta' = \theta - \theta_i$ and the small angle approximation $\sin \theta' \approx \theta', \cos \theta' \approx 1$ into (13), the phase term becomes

$$2\mathbf{k} \cdot (\mathbf{r}' - \mathbf{r}) - ka(\theta - \theta_c)^2 \approx -k(a\theta'^2 + 2p\theta' + 2q), \quad (14)$$

with

$$\begin{aligned} p &= (x' - x) \sin \theta_i - (y' - y) \cos \theta_i + a(\theta_i - \theta_c), \\ q &= -(x' - x) \cos \theta_i - (y' - y) \sin \theta_i + a(\theta_i - \theta_c)^2/2. \end{aligned}$$

Thus, the position \mathbf{r}' of the imaged pixels can be represented as

$$\mathbf{r}' = \mathbf{r} + \bar{\mathbf{T}}(\theta_i) \cdot \mathbf{r}_{\text{shift}}(\theta_i) - \bar{\mathbf{T}}(\theta_i) \cdot [q, p]^T, \quad (15)$$

where first and second terms on the right side represent scattering center position and shift, respectively.

If the imaging grids are sufficiently dense, the third term on the right-hand side of (15) can be neglected as $q = p = 0$. It yields

$$\mathbf{r}' = \mathbf{r} + \bar{\mathbf{T}}(\theta_i) \cdot \mathbf{r}_{\text{shift}}(\theta_i). \quad (16)$$

Then, Eq. (13) becomes

$$s(\theta_i, \mathbf{r}') = A \delta(\mathbf{r}' - \mathbf{r} - \bar{\mathbf{T}} \cdot \mathbf{r}_{\text{shift}}) \int \exp[-(\theta_i + \theta' - \theta_o)^2/2\sigma^2 - \theta'^2/2\sigma_y^2] \exp(-ika\theta'^2) d\mathbf{k}, \quad (17)$$

where $\delta(\cdot)$ is the Dirac delta function.

Table 2 Parameters of the six objects used for validating the model.

Object	Position (m)	Length (m)	Height (m)	Radius (m)	Orientation (°)
Dihedral1	(-3.5, 3.5)	0.6	0.1	-	5
Dihedral2	(3.5, 3.5)	0.6	0.1	-	-8
Cylinder1	(0, 0)	0.9	-	0.15	0
Cylinder2	(3.5, 3.5)	0.9	-	0.15	4
Sphere	(-3.5, -3.5)	-	-	0.5	-
Trihedral	(3.5, -3.5)	-	0.08	-	0

5 Experimental validation

5.1 Simulation of simple geometric objects based on the scattering models

Scattering from simple geometric objects, such as dihedral, trihedral, cylinder, and sphere, can be calculated analytically [11]. To test the model, we assumed six objects that were located on a plane, as shown in Figure 6(a), with sizes and locations listed in Table 2. Note that dihedral2 and cylinder2 are closely located in Figure 6(a). In this test, the center frequency was 10 GHz, the bandwidth was 500 MHz, and the azimuthal synthetic aperture was 30°. There were 500 and 100 sampling points for the frequency and azimuth, respectively, and these points were distributed evenly. The wide-angle imaging of the total aperture is shown in Figure 6(b), and these results were obtained using the back-projection (BP) algorithm.

The scattering data for these objects were transformed into a group of spectrograms using sequential Gabor imaging. To obtain the resolution of 0.3 m in the cross-range direction, σ_g was calculated using (11). The azimuthal angles $\theta_1, \theta_2, \dots, \theta_N$ were sampled uniformly in the $[-15^\circ + \sigma_g, 15^\circ - \sigma_g]$ interval, and the number of sampling points was $N_\theta = 25$. Figure 7 (a) and (b) show the amplitude and the phase of spectral lines for the six imaged objects, at their center positions.

The results show that the spectral amplitudes of dihedral1, cylinder1, and trihedral objects follow Gaussian curves, but the spectral phases appear to remain invariant in the azimuth. Specifically, the spectral amplitude and phase of the sphere follow Gaussian curves and its amplitude variance is large, because scattering from a sphere is isotropic in the azimuthal direction, making its spectral lines in Gaussian-distributed and sliding the scattering center.

It can also be seen that the scattering curves for dihedral2 and cylinder2 are at the same location, but have different orientations, exhibiting two peaks for the spectral amplitudes (Figure 7(a), dih-cyl) and a step-like change in the spectral phases (Figure 7(b)).

Based on the results, it can be concluded that large-variance Gaussian amplitudes represent wide-angle persistence, and the spectral phase, being either a line or a curve, indicates a planar-surface or curved-surface scatterer, respectively. The number of amplitude peaks may indicate the number of objects at the same imaging position. The phase variation can also indicate whether it is caused by a larger number of scatterers.

5.2 Scattering classification of a backhoe

The wide-angle scattering data of a backhoe at X-band [21] were employed to validate the GAP model. The wideband data were chosen with the span [8.5, 11.5 GHz] from the azimuthal angle of 80° to that of 100°, under nadir observation. Figure 8 (a) and (b) show the backhoe model and the results of its wide-angle imaging.

A sequential Gabor transform was adopted for the backhoe data, with $\sigma_g = 0.0707$ and $N_\theta = 30$. Three points, P1, P2, and P3, in Figure 8(b) were specifically chosen for comparing the GAP model results to the data, and the comparison results are shown in Figure 9. The point P1 is at the scoop side edge and it shows planar scattering from the scoop side surface, which coincides with the linear invariant phase (blue curve) in Figure 9(a). The point P2 contains the bracket and others and yields two spectral amplitude peaks. The point P3 is seen on a wheel, which can be validated by the Gaussian phase in Figure 9(b).

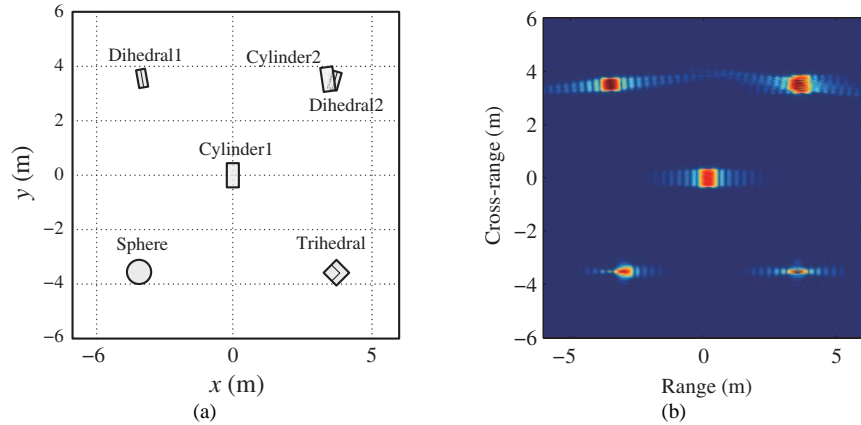


Figure 6 (Color online) Wide-angle imaging of six objects. (a) Locations of objects; (b) imaging results.

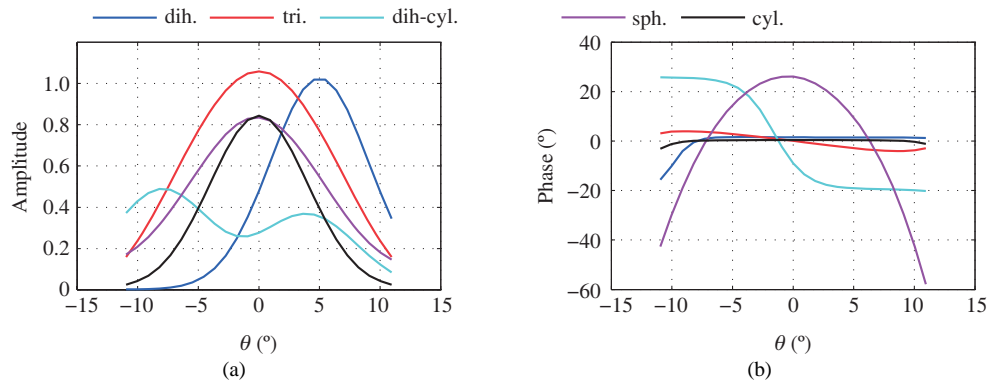


Figure 7 (Color online) Azimuthal spectral lines for six objects. (a) Amplitude; (b) phase.

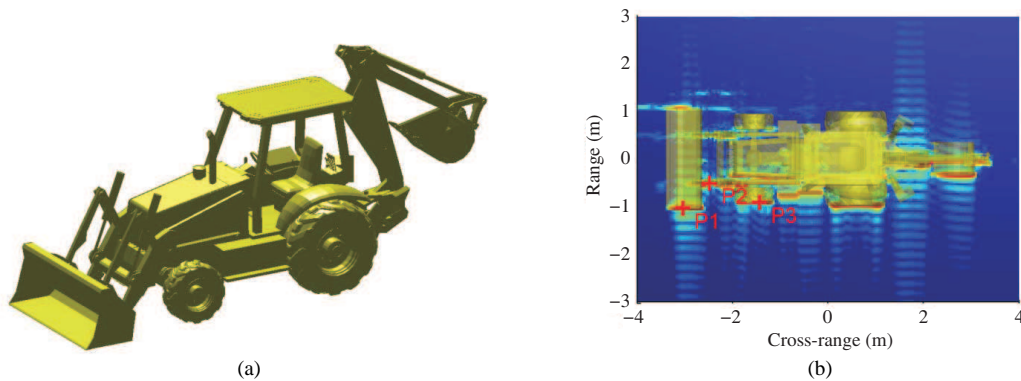


Figure 8 (Color online) The backhoe model and the results of wide-angle imaging. (a) The backhoe model; (b) wide-angle imaging.

Figure 10 shows the GAP model parameters obtained after processing all imaged pixels with amplitudes above 5 dB. Figure 10(a) shows the scattering mechanisms, i.e., the number of objects, which coincides with the backhoe model (e.g., the front and back scoop sides), and two or more objects account for high-order scattering from the backhoe. The normalized σ/σ_g in Figure 10(b) can be categorized into three regions to represent glint, narrow-angle, and persistent scattering, respectively. In Figure 10(c), based on the parameter a , the objects are categorized as planar-surface or curved-surface ones. Certainly, the classification in Figure 10 (a)–(c) might be only a rough indication of the attributes affected by scattering, such as the shape of an object, its orientation, type, and intersection.

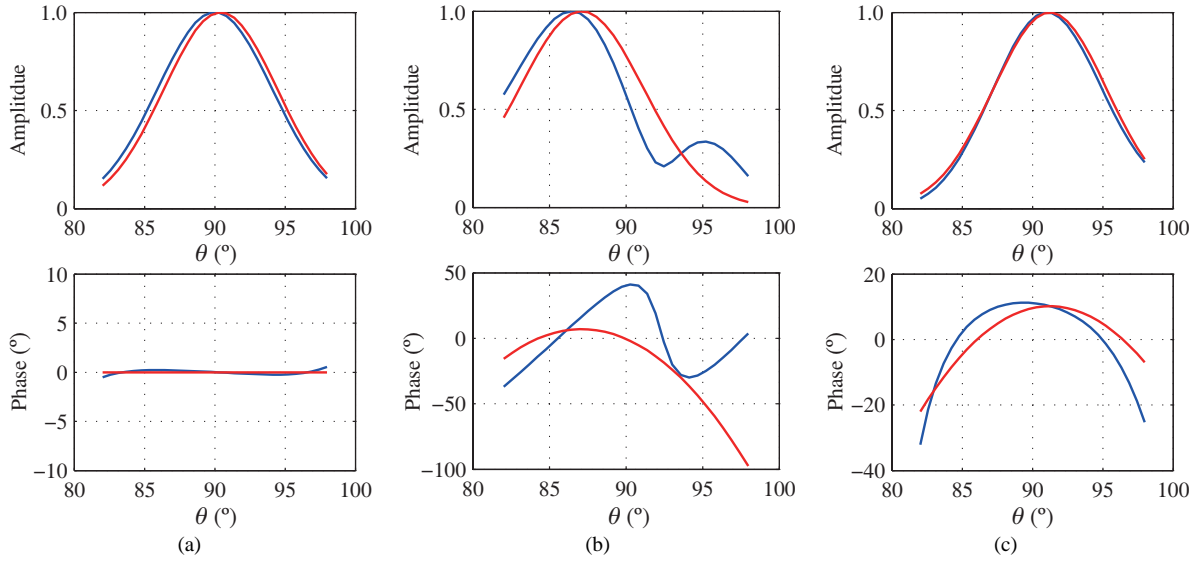


Figure 9 (Color online) Spectrograms of three points for the backhoe model (blue curves: the spectrograms, red curves: the GAP model estimations). (a) P1; (b) P2; (c) P3.

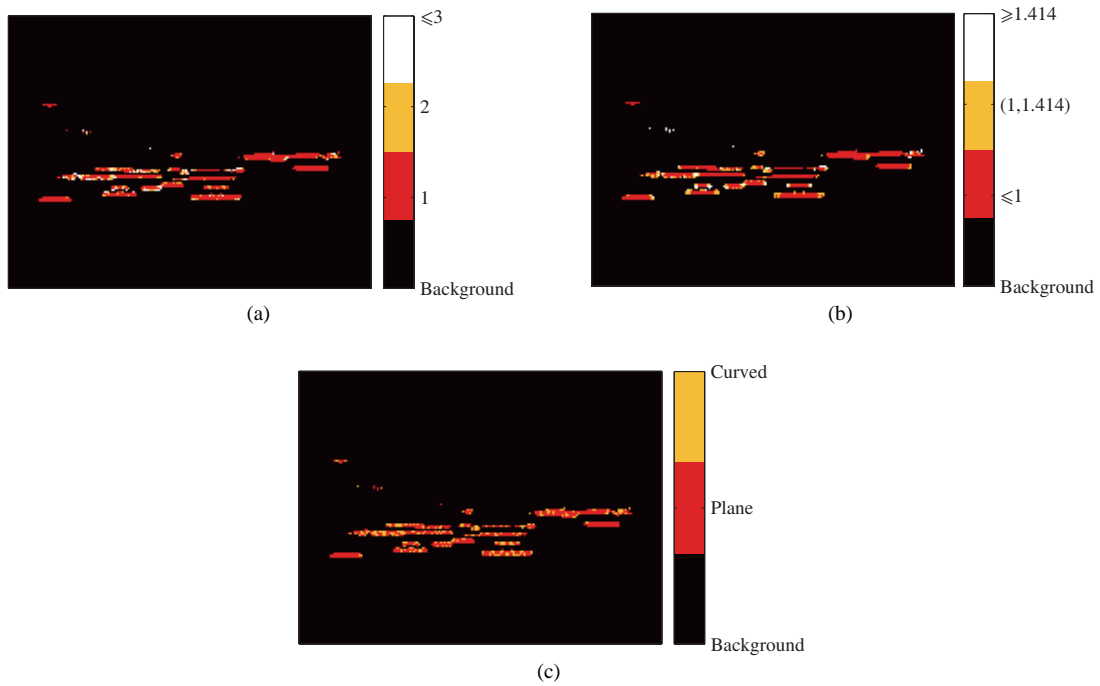


Figure 10 (Color online) Pixel classification of backhoe imaging. (a) Number of objects (red: 1, yellow: 2, white: 3 or more); (b) scattering persistence (red: $\sigma/\sigma_g \leq 1$, yellow: $1 < \sigma/\sigma_g < \sqrt{2}$, white: $\sqrt{2} \leq \sigma/\sigma_g$); (c) scatterer type (red: planar-surface object, $a \leq \lambda/2$; yellow: curved-surface object $a > \lambda/2$).

5.3 Scattering classification of a scaled vessel

As another example, the 1/50 scaled model of a vessel in Figure 2 was adopted for demonstrating scattering classification. The parameters of this vessel model, measured in a chamber, were the 147–153 GHz frequency span and the 85°–95° azimuthal span, with an elevation angle of 45°. The frequency sampling step was 7.5 MHz and the azimuthal sampling step was 0.01°. The results of the scattering-based imaging of the vessel model, obtained using the BP algorithm, are shown in Figure 11.

Using the Gabor window parameters $\sigma_g = 0.05$ and $N_\theta = 25$, a sequential Gabor transform was adopted for obtaining the vessel’s spectrogram. Similarly, three points in Figure 11, P1, P2, and P3,

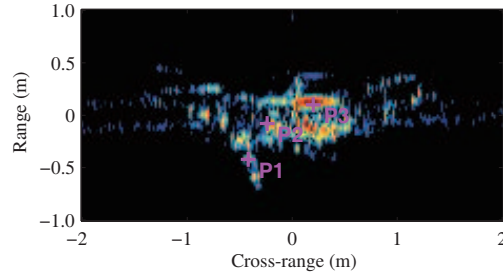


Figure 11 (Color online) Imaging of the scaled vessel model.

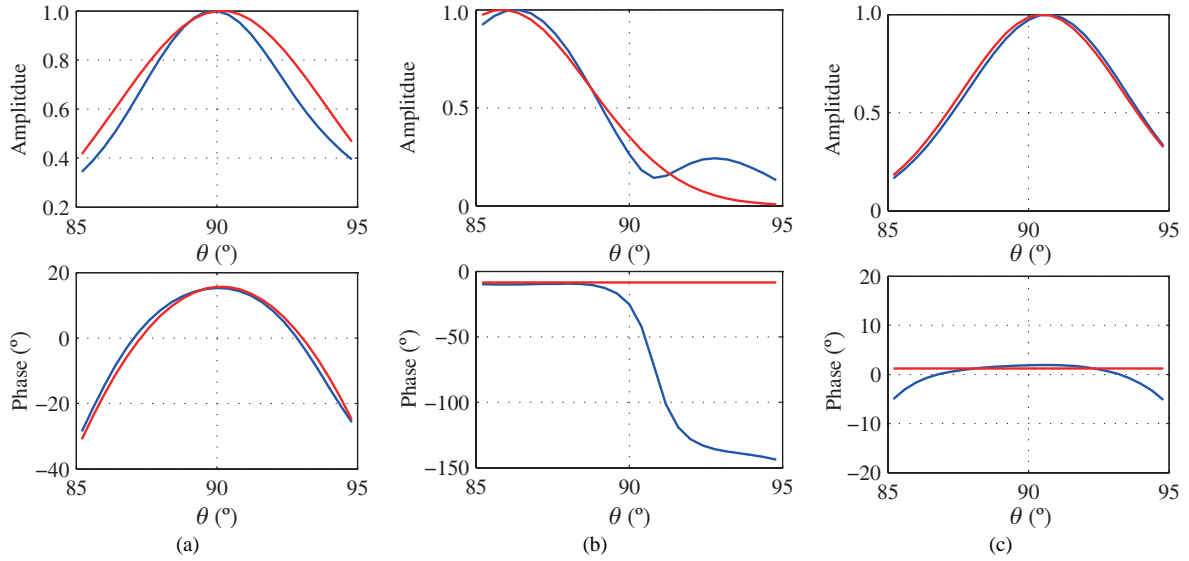


Figure 12 (Color online) Spectrograms for three points in the vessel model (blue curves: the spectrograms, red curves: the GAP model estimations). (a) P1; (b) P2; (c) P3.

were chosen for analysis. Figure 12 (a)–(c) show the comparison of spectrograms (blue curves for data, and red curves for the GAP model). The points P1, P2, and P3 represent one curved-surface object, two overlapping objects, and one planar-surface object, respectively. Even though the estimation is quite rough, P1 indicates a curved-surface object on a tower, P2 indicates the front chimney, and P3 indicates a dihedral geometry on the bottom of the back chimney.

Figure 12 shows that the GAP model results are in a good correspondence with the actual data. In Figure 13, the vessel imaging data for pixel amplitudes above -10 dB are plotted for the number of objects, normalized scattering persistence σ/σ_g , and object type.

The vessel complexity imposes serious layover in imaging, and most of the imaged pixels contain more than one object, as shown in Figure 13(a). In addition, the dominant scattering scatterers significantly change with the azimuth, which actually causes more objects to be associated with one pixel. According to the component decomposition of the vessel model in Figure 2, the vessel is seen as composed of many simple geometric objects. Owing to the diversity of the scattering persistence of different objects, the classification in term of the scattering persistence and object type in Figure 13 (b) and (c) only presents a rough interpretation of the vessel model.

6 Conclusion

Wide-angle synthetic aperture radar (W-SAR) scattering and imaging involve diverse patterns of scattering, as evident from wide azimuthal angles. Based on the decomposition of electric-large complex targets into simple objects (as main components), the Gaussian amplitude-phase (GAP) model in the time domain called the parametric spectrogram was derived for characterizing azimuthal scattering from simple

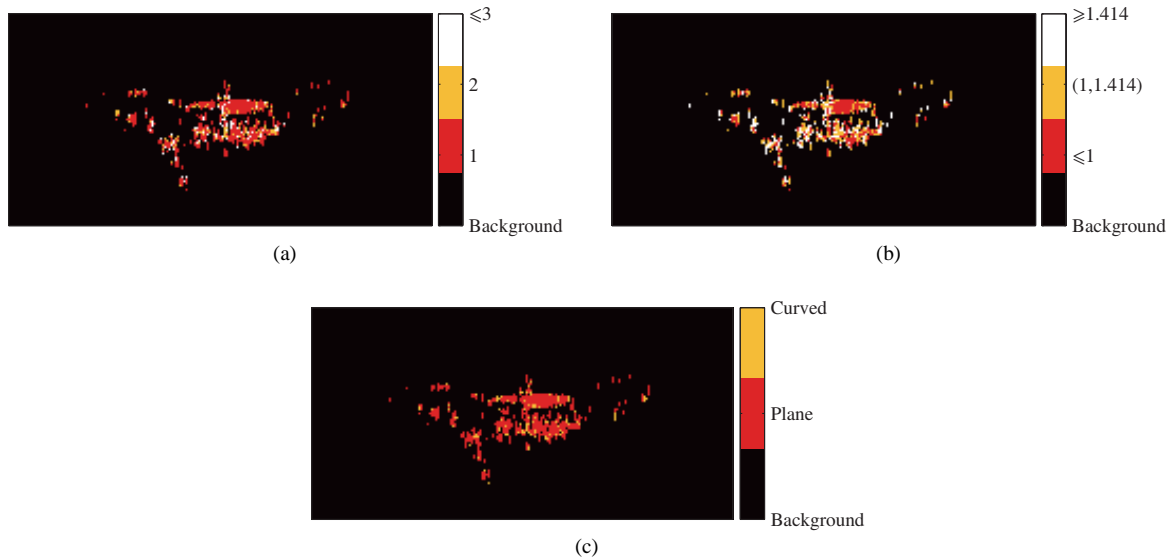


Figure 13 (Color online) Pixel classification of vessel imaging. (a) The number of objects (red: 1, yellow: 2, white: 3 or more); (b) scattering persistence (red: $\sigma/\sigma_g \leq 1$, yellow: $1 < \sigma/\sigma_g < \sqrt{2}$, white: $\sqrt{2} \leq \sigma/\sigma_g$); (c) scatterer type (red: planar-surface object, $a \leq \lambda/2$; yellow: curved-surface object $a > \lambda/2$).

geometric objects. Using the Gabor transform, the parameters of the GAP model, such as the scattering persistence, orientation, the number and type of the objects in the imaged pixels, were estimated using the OMP algorithm. Experimental W-SAR data of a backhoe and a vessel model were employed for validating the GAP model performance on object classification tasks.

Acknowledgements This work was supported by National Natural Science Foundation of China (Grant No. 61471127) and Shanghai Yangpu Ding-Yuan Foundation. Y. C. Li is grateful to Dr. A.S. Khwaja for useful discussion on GAP.

Conflict of interest The authors declare that they have no conflict of interest.

References

- Moses R L, Potter L C, Çetin M. Wide-angle SAR imaging. In: Proceedings of SPIE in Algorithms for Synthetic Aperture Radar Imagery XI, Orlando, 2004. 5427: 164–175
- Lanterman A, Munson D, Wu Y. Wide-angle radar imaging using time-frequency distributions. IEE Proc-Radar Sonar Navig, 2003, 150: 203–211
- Ash J N, Ertin E, Potter L C, et al. Wide-angle synthetic aperture radar imaging: models and algorithms for anisotropic scattering. IEEE Signal Process Mag, 2014, 31: 16–26
- Ferro-Famil L, Reigber A, Pottier E, et al. Scene characterization using subaperture polarimetric SAR data. IEEE Trans Geosci Remote Sens, 2003, 41: 2264–2276
- Duquenoy M, Ovarlez J-P, Ferro-Famil L, et al. Scatterers characterisation in radar imaging using joint time-frequency analysis and polarimetric coherent decompositions. IET Radar Sonar Navig, 2010, 4: 384–402
- Duquenoy M, Ovarlez J-P, Ferro-Famil L, et al. Characterization of scatterers by their energetic dispersive and anisotropic behaviors in high-resolution laboratory radar imagery. In: Proceedings of IEEE International Geoscience and Remote Sensing Symposium (IGARSS), Quebec, 2014. 4715–4718
- Spigai M, Tison C, Souyris J-C. Time-frequency analysis in high-resolution SAR imagery. IEEE Trans Geosci Remote Sens, 2011, 49: 2699–2711
- Dungan K E, Potter L C. Classifying vehicles in wide-angle radar using pyramid match hashing. IEEE J Sel Top Signal Process, 2011, 5: 577–591
- Fuller D F, Saville M A. A high-frequency multipole model for wide-angle SAR imagery. IEEE Trans Geosci Remote Sens, 2013, 51: 4279–4291
- Zhao Y, Lin Y, Hong W, et al. Adaptive imaging of anisotropic target based on circular-SAR. Electron Lett, 2016, 52: 1406–1408
- Jackson J A, Rigling B D, Moses R L. Canonical scattering feature models for 3D and bistatic SAR. IEEE Trans Aerosp Electron Syst, 2010, 46: 525–541
- Rihaczek A W, Hershkowitz S J. Radar Resolution and Complex-Image Analysis. Norwood: Artech House, Inc., 1996

- 13 Jackson J A, Moses R L. Synthetic aperture radar 3D feature extraction for arbitrary flight paths. *IEEE Trans Aerosp Electron Syst*, 2012, 48: 2065–2084
- 14 Trintinalia L C, Bhalla R, Ling H. Scattering centre parameterization of wide-angle backscattered data using adaptive Gaussian representation. *IEEE Trans Antennas Propag*, 1997, 45: 1664–1668
- 15 Li J, Ling H. Application of adaptive chirplet representation for ISAR feature extraction from targets with rotating parts. *IEE Proc-Radar Sonar Navig*, 2003, 150: 284–291
- 16 Leducq P, Ferro-Famil L, Pottier E. Matching-pursuit-based analysis of moving objects in polarimetric SAR images. *IEEE Geosci Remote Sens Lett*, 2008, 5: 123–127
- 17 Qian S E, Chen D P. Joint time-frequency analysis. *IEEE Signal Process Mag*, 1999, 16: 52–67
- 18 Çetin M, Ivana S, Onhon N O, et al. Sparsity-driven synthetic aperture radar imaging: reconstruction, autofocusing, moving targets, and compressed sensing. *IEEE Signal Process Mag*, 2014, 31: 27–40
- 19 Davis G, Mallat S, Avellaneda M. Adaptive greedy approximations. *Constr Approx*, 1997, 13: 57–98
- 20 Potter L C, Ertin E, Parker J T, et al. Sparsity and compressed sensing in radar imaging. *Proc IEEE*, 2010, 98: 1006–1020
- 21 Naidu K, Lin L. Data Dome: full k-space sampling data for high-frequency radar research. In: *Proceedings of SPIE in Algorithms for Synthetic Aperture Radar Imagery XI*, Orlando, 2004. 5427: 200–207

Appendix A Calculation of (17)

Eq. (17) is a double integral over both the frequency and the azimuthal angle. Replacing k by the central frequency k_c , Eq. (17) becomes a single integral over θ' ,

$$s(\theta_i, \mathbf{r}') = A' \delta(\mathbf{r}' - \mathbf{r} - \bar{\mathbf{T}} \cdot \mathbf{r}_{\text{shift}}) \int \exp[-(\theta_i + \theta' - \theta_o)^2/2\sigma^2 - \theta'^2/2\sigma_g^2] \exp(-ik_c a \theta'^2) d\theta'. \quad (\text{A1})$$

It is known that

$$\int_{-\infty}^{\infty} \exp(-tx^2) dx = \sqrt{\pi/t}. \quad (\text{A2})$$

It can be seen that the Gabor function has a Gaussian window, which makes the amplitude of the Gabor function decrease exponentially with increasing $|\theta'|$. Beyond the span of $\theta' = \pm 3\sigma_g$, the amplitude quickly decreases to less than 1% of the maximum. Thus, it remains only to integrate over a limited range of $|\theta'|$.

Defining $\alpha = 1/\sigma^2$, $\beta = 1/\sigma_g^2$, $\gamma = 2k_c a$, with variable substitution, Eq. (A1) becomes

$$s(\theta_i, \mathbf{r}') = A' \delta(\mathbf{r}' - \mathbf{r} - \bar{\mathbf{T}} \cdot \mathbf{r}_{\text{shift}}) \int \exp[-(\alpha + \beta + i\gamma)\theta'^2/2 - \alpha(\theta_i - \theta_o)\theta' - \alpha(\theta_i - \theta_o)^2/2] d\theta'. \quad (\text{A3})$$

Substituting $t_1 = (\alpha + \beta + i\gamma)/2$, $t_2 = \alpha(\theta_i - \theta_o)/2$, $t_3 = \alpha(\theta_i - \theta_o)^2/2$ into (A3), it becomes

$$\begin{aligned} s(\theta_i, \mathbf{r}') &= A' \delta(\mathbf{r}' - \mathbf{r} - \bar{\mathbf{T}} \cdot \mathbf{r}_{\text{shift}}) \int \exp(-t_1 \theta'^2/2 - 2t_2 \theta' - t_3) d\theta' \\ &= A' \delta(\mathbf{r}' - \mathbf{r} - \bar{\mathbf{T}} \cdot \mathbf{r}_{\text{shift}}) \int \exp(-t_1(\theta'^2 + t_2/t_1)^2 + t_2^2/t_1 - t_3) d\theta'. \end{aligned} \quad (\text{A4})$$

Then, Eq. (A4) can be approximately calculated as

$$s(\theta_i, \mathbf{r}') \approx A' \sqrt{\pi/t_1} \exp(t_2^2/t_1 - t_3) \delta(\mathbf{r}' - \mathbf{r} - \bar{\mathbf{T}} \cdot \mathbf{r}_{\text{shift}}). \quad (\text{A5})$$

Finally, substituting t_1, t_2, t_3 into (A5), we obtain

$$s(\theta_i, \mathbf{r}') = A' \exp[-(\nu_1 + i\nu_2)(\theta_i - \theta_o)^2] \delta(\mathbf{r}' - \mathbf{r} - \bar{\mathbf{T}} \cdot \mathbf{r}_{\text{shift}}), \quad (\text{A6})$$

with

$$\nu_1 = \frac{\alpha(\alpha\beta + \beta^2 + \gamma^2)}{2[(\alpha + \beta)^2 + \gamma^2]}, \quad \nu_2 = \frac{\alpha^2\gamma}{2[(\alpha + \beta)^2 + \gamma^2]},$$

where A' has combined a amplitude $\sqrt{2\pi/(\alpha + \beta + i\gamma)}$.